THE JOURNAL OF PHYSICAL CHEMISTRY C

Article

pubs.acs.org/JPCC

Solid-State NMR Investigations of $MgCl_2$ Catalyst Support

E. S. (Merijn) Blaakmeer,[†,‡] Giuseppe Antinucci,[‡,§] Vincenzo Busico,[‡,§] Ernst R. H. van Eck,[†] and Arno P. M. Kentgens*[,†]

[†]Institute for Molecules and Materials, Radboud University, Heyendaalseweg 135, 6525 AJ Nijmegen, The Netherlands

[‡]Dutch Polymer Institute (DPI), P.O. Box 902, 5600 AX Eindhoven, The Netherlands

[§]Laboratory of Stereoselective Polymerizations, Federico II University of Naples, Via Cintia, 80126 Naples, Italy

Supporting Information

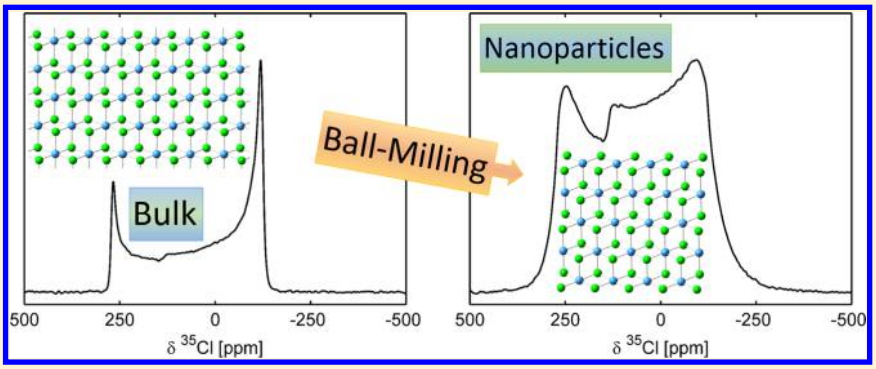

ABSTRACT: $MgCl_2$ is a vital component of Ziegler–Natta catalysts for olefin polymerization. Here we synthesized anhydrous $MgCl_2$ using different drying protocols and exploited ^1H NMR to quantify the proton content. We report on our study of neat and ball-milled $MgCl_2$ samples by means of ^{25}Mg and ^{35}Cl solid-state NMR. DFT calculations of the quadrupole tensor aid in analysis of the spectra. The results show that, due to the morphology of the neat particles, a preferred orientation is induced which manifests itself in unusual powder line shapes. Ball milling reduces particle size, which subsequently leads to a small distribution of quadrupole parameters for the bulk. Surface sites, highly relevant for catalysis, are not directly observed, due to their broad lines of low intensity.

INTRODUCTION

Supported Ziegler–Natta catalysts (ZNCs) are used for the commercial production of stereoregular polyolefins. They account for a majority of the stunning amount of over 130 million tons of polyolefins that are produced annually.[1] The titanium-based catalytic systems were introduced by Ziegler and Natta in the 1950s[2,3] and have significantly evolved since then. Nowadays ZNCs are composed of the following components: $MgCl_2$ support, $TiCl_4$ catalyst, organoaluminum cocatalyst, and internal/external electron donors.

The use of $MgCl_2$ as a support material was introduced by Kashiwa in the late 1960s,[4] and it has been an important component of the catalyst system ever since. The common polymorph of $MgCl_2$ (α-$MgCl_2$) crystallizes in the $R\bar{3}m$ space group.[5] The structure consists of Cl–Mg–Cl triple layers along the c axis. The surfaces perpendicular to this axis expose unsaturated magnesium sites which are relevant for catalysis. To obtain a large surface area, essential for efficient catalysis, $MgCl_2$ is chemically or physically activated. In the latter case, α-$MgCl_2$ is ball milled for several hours, resulting in nanoparticles known as the δ-phase.[6−8] It can be formed chemically from $MgCl_2R_x$ adducts via the elimination of Lewis bases (R = ethyl acetate, ethyl benzoate, ethyl p-methoxybenzoate, ethyl p-buthoxybenzoate, ethanol, etc.)[9−11] or directly from metallic magnesium and alkyl chloride.[12] The surfaces are stabilized by organic electron donors, which also aid in increasing the catalysts' activity and/or stereoselectivity by selective coordination to particular sites.

Although known for a long time, ZNCs are still poorly understood at the molecular level. The unambiguous identification of the structure and dynamics of the active sites would evidently set the premise for a more rational catalyst design and improvement, e.g., by predicting the right combination of donors to get the desired performance. It is very difficult to obtain detailed information from experiments because these solids are extremely reactive, generally very disordered, and have complex compositions. Since solid-state nuclear magnetic resonance (NMR) does not put any constraints on the physical appearance of the sample, it makes this technique suitable to study the heterogeneous systems.

This paper is a first step aimed at investigating the exact structure and mechanistic operation of Ziegler–Natta catalysts using solid-state NMR. In order to be able to understand

Received: December 24, 2015
Revised: February 27, 2016
Published: February 29, 2016

DOI: 10.1021/acs.jpcc.5b12606
J. Phys. Chem. C 2016, 120, 6063−6074

interactions between the different components and the support, it is important to first fully understand the support itself. To this end, we report here on the investigation of the neat support material, $MgCl_2$, activated by ball milling by means of both ^{25}Mg and $^{35,37}Cl$ quadrupolar solid-state NMR. We support our findings by DFT calculations of the ^{25}Mg and ^{35}Cl quadrupolar tensor.

Quadrupolar broadened spectra are a valuable source of information for structural investigations. As far back as 1988, Dupree et al.[13] reported on the value of ^{25}Mg ($I = 5/2$) NMR in structural investigations. Indeed, magnesium NMR has been applied in the study of minerals, glasses, and other inorganic compounds[14−20] as well as metals, intermetallics,[21] and organic compounds.[22,23] Recent studies[24−27] show the potential of modern ^{25}Mg investigations. The studies have shown that chemical shifts are usually in a moderately narrow chemical shift range of 40 ppm, and quadrupolar interactions are often below 5 MHz and only seldom exceed 10 MHz.

While reports on magnesium NMR remain scarce, chlorine NMR has gained more interest in recent years as evidenced by a number of recent papers employing the combination of high magnetic fields with DFT calculations and/or NQR spectroscopy for the study of chlorine in various organometallic complexes.[28−31] They exhibit extremely broad spectra for both ^{35}Cl ($I = 3/2$) and ^{37}Cl ($I = 3/2$) isotopes, which were also found for covalently bound chlorine in organic compounds.[32] However, the review of Chapman et al.[33] shows that chlorine can be more easily accessible for other classes of materials such as inorganic chloride salts,[34,35] perchlorates,[36] and organic chloride salts and hydrochlorides.[37−41]

Notwithstanding the potential of ^{25}Mg and ^{35}Cl solid-state NMR discussed in the examples above, these nuclei are not commonly studied due to sensitivity issues. Despite advances in magnetic field strength and signal enhancement techniques, the acquisition of high-quality ^{25}Mg and ^{35}Cl spectra often remains challenging.

Vittadello et al.[42] reported static ^{35}Cl spectra for α-$MgCl_2$ and δ-$MgCl_2$. They measured a single site for α-$MgCl_2$ which could be simulated using a quadrupolar coupling constant of 4.58 MHz. For the δ-phase they observed a distribution in quadrupolar parameters which was modeled with a Lorentzian function. A ^{25}Mg spectrum of $MgCl_2$ has been published by Pallister et al.[24] They showed a ^{25}Mg MAS spectrum and reported a single site at $\delta_{iso} = 2.3$ ppm with quadrupolar parameters $C_Q = 1.62 \pm 0.02$ and $\eta = 0.00 \pm 0.05$. However, in both studies there is a discrepancy between the simulation and the experimental spectrum, which is not discussed by the authors.

Nominal anhydrous $MgCl_2$ as received from the suppliers contains a significant amount of water, which can be detected as different hydrate phases in powder X-ray diffraction (XRD). Due to its strong adsorption to the surface[43] it might block sites for catalysis. It is therefore important to come up with a method to obtain dry $MgCl_2$ and work under a controlled atmosphere. Therefore, we introduce a new chemical drying procedure and performed static ^1H measurements to quantify the proton content. Most of the work discussed in this paper is focused on samples prepared via this chemical drying protocol. We also tested a second drying protocol that is based on calcination of $MgCl_2$.

In this paper we report on our ^{25}Mg and $^{35,37}Cl$ NMR investigations of a series of $MgCl_2$ samples. We explain the origin of the line shape observed in the ^{25}Mg and $^{35,37}Cl$ MAS NMR spectra and present the spectral changes upon ball milling of the sample. We also discuss the effect of H_2O in the system using ^1H MAS NMR and static ^1H NMR experiments performed in a home-built proton-free probehead. Finally, we show the implementation of signal enhancement techniques to obtain spectra with a higher signal-to-noise ratio in less time.

RESULTS

Dry $MgCl_2$. We implemented a newly developed drying protocol consisting of a treatment of $MgCl_2$ in aliphatic hydrocarbon slurry, with $SiCl_4$. ICP-OES showed that some silicon was still present after washing (see Experimental Section). From EDS-TEM analysis we concluded that this is most likely present in the form of silica nanoparticles. The XRD patterns, see Figure SI 1, show how chemical drying successfully removes crystalline hydrate phases. However, XRD cannot detect water present in amorphous phases and on the surfaces. To this end, we employed solid-state ^1H NMR. A second drying protocol was also tested. This involved calcination of $MgCl_2$ in a flow of dry nitrogen at 250 °C. An overview of the resulting $MgCl_2$ samples, of which the synthesis is described in the Experimental Section in more detail, is given in Table 1.

Table 1. Primary Samples Investigated in This Study

samples code	drying protocol	ball milled (y/n)
dried $MgCl_2$/$MgCl_2$ D	$SiCl_4$	n
dried and ball-milled $MgCl_2$/$MgCl_2$ DM	$SiCl_4$	y
dried $MgCl_2$/$MgCl_2$ DC	calcination	n
dried and ball-milled $MgCl_2$/$MgCl_2$ DCM	calcination	y

The full-width at half-height of the 001 ($2\theta \approx 15°$) and 110 ($2\theta \approx 50°$) diffraction peaks, see Figure SI 2, can be used to get the particle size of $MgCl_2$ nanoparticles obtained after ball milling.[8] The average primary particle size in the basal planes ($\langle L_a \rangle$) and perpendicular to them ($\langle L_c \rangle$) for $MgCl_2$ DM is found to be 12.6 and 13.0 nm. For $MgCl_2$ DCM it is 14.6 and 16.1 nm, respectively.

In all samples ^1H NMR shows a significant proton signal, Figure 1, which corresponds to the equivalent of 3.5% and 5.5% of H_2O per Mg for $MgCl_2$ D and $MgCl_2$ DM, respectively. At most 10% of the proton signal might result from silanol groups at the surface of residual silica particles. The proton line has a

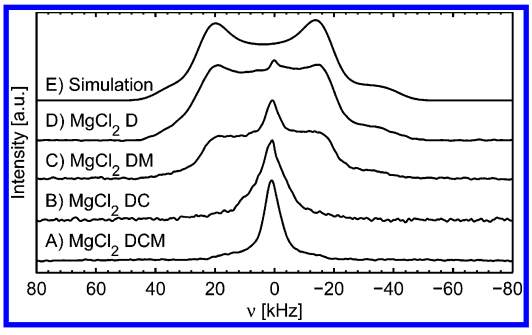

Figure 1. Experimental static Hahn-echo ^1H NMR spectra obtained at 7.1 T of (A) $MgCl_2$ DCM, (B) $MgCl_2$ DC, (C) $MgCl_2$ DM, and (D) $MgCl_2$ D, and (E) simulation of Pake doublet (isolated proton pair) with $r_{H-H} = 1.65$ Å, 20 ppm of CSA, and 10 kHz Gaussian line broadening.

DOI: 10.1021/acs.jpcc.5b12606
J. Phys. Chem. C 2016, 120, 6063−6074

distinctive shape indicating a Pake doublet.[44] There are other, more narrow, components as well which represent minor fractions of mobile or isolated protons.

The proton content of the calcinated samples is lower, corresponding to the equivalent of 1% H_2O for $MgCl_2$ DC and 4.5% for $MgCl_2$ DCM. Importantly, the proton spectrum changed dramatically compared to the chemically dried samples, see Figure 1. The spectrum of $MgCl_2$ DCM is dominated by a narrow line with a fwhm of 6 kHz. A second, broader component is also present but with a significantly lower intensity and no longer appearing as a Pake doublet. For $MgCl_2$ DC there is only one relatively narrow resonance of 11 kHz wide.

To further elucidate the nature of the proton signal we resorted to MAS experiments in order to resolve isotropic chemical shifts. MAS experiments spinning at 15.625 kHz (see Figure SI 4) show a narrow line around 1.7 ppm with a shoulder on the right-hand side (at 1.3 ppm) for $MgCl_2$ DCM. A broader shoulder is detected around 3.5 ppm. The DC sample shows these resonances as well, although with lower intensity. The chemically dried samples have their peak maximum around 5 ppm. For $MgCl_2$ DM the main peak is found at 4.5 ppm, but there is also a small peak at 1.8 ppm. $MgCl_2$ D shows a bicomponent line shape consisting of peaks at 5.2 and 3.5 ppm. It lacks a narrow signal below 2 ppm.

The intermediate spinning speed of 15.625 kHz might not have been fast enough to average the dipolar interactions for $MgCl_2$ D and DM. Therefore, we finally performed fast MAS (50 kHz) experiments in an attempt to further resolve the separate resonances. The results can be seen in Figure 2 for the

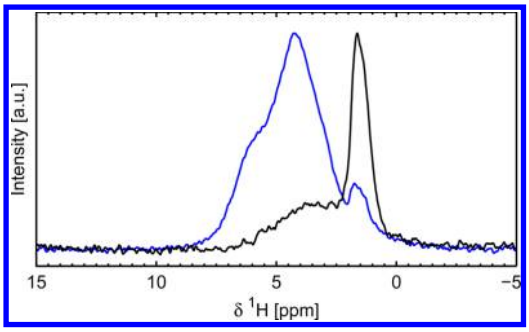

Figure 2. Experimental 50 kHz MAS ^{1}H NMR spectra of $MgCl_2$ DM (blue) and $MgCl_2$ DCM (black) at 20 T.

ball-milled samples. For $MgCl_2$ DM the major component is found at 4.1 ppm. There is also a shoulder at 6.2 ppm and a small component at 1.6 ppm. For $MgCl_2$ DCM the resonance at 1.6 ppm is the main component, although this is actually composed of two peaks: one at 1.7 and one at 1.4 ppm. There is also a broader component at 3.5 ppm.

Neat $MgCl_2$. At 20T, $MgCl_2$ D shows a ^{35}Cl MAS NMR spectrum which is about 150 ppm wide, see Figure 3. The observed line shape is very unusual for a quadrupolar nucleus. The resonance is composed of two sharp peaks and a broad shoulder on the right side of the two peaks. Comparing the experimental line shape of $MgCl_2$ with a theoretical spectrum for a quadrupolar nucleus (δ_{iso} = 131 ppm, C_Q = 4.61 MHz, and η = 0, in agreement with the result reported by Vittadello et al.[42]) shows the good agreement between the discontinuities and the peak positions. The experimental intensities, on the other hand, are rather different from the simulated ones. The differences are most striking for the broad shoulder, which is

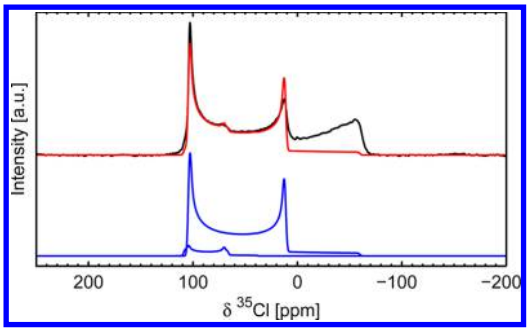

Figure 3. ^{35}Cl NMR (31.25 kHz MAS) spectrum of $MgCl_2$ at 20 T (black); simulated theoretical spectrum (red) with individual components (blue).

only a low-intensity foot in the simulated spectrum. To check that experimental RF settings did not cause line shape distortions, the theoretical spectrum was simulated using the experimental RF field strength including excitation effects. The simulation also includes an unknown impurity (δ_{iso} = 118 ppm, C_Q = 2.97 MHz, and η = 0.11) which accounts for a few percent of the total intensity.

Similar observations can be made for the static spectra of $MgCl_2$ D, see Figure SI 5. A theoretical line fits well with the position of the singularities and discontinuities in the experimental spectrum, but the intensities are less satisfactorily accounted for. The discrepancy mainly concerns the left peak, although the mismatch is not as drastic as for the MAS spectrum.

To shed more light on the unusual line shape, we performed measurements at a lower magnetic field of 14.1 T (see Figures SI 6–8). These show that the width of the ^{35}Cl MAS NMR spectrum of $MgCl_2$ D increases inversely proportional to the field strength, but the line shape remains exactly the same. The $1/B_0$ field dependency indicates that the line shape is solely the result of the quadrupolar interaction. This is corroborated by ^{37}Cl MAS NMR measurements, which also show the same line shape (Figures SI 9 and 10). Moreover, a ^{35}Cl MQMAS experiment (Figure SI 11) shows that the line shape cannot be attributed to the existence of multiple components in the sample.

Magnesium resides in an octahedral site which is slightly distorted;[5] as a consequence there is a small quadrupolar interaction. The ^{25}Mg MAS NMR spectrum of $MgCl_2$ shows the same remarkable distorted quadrupolar line shape as the ^{35}Cl spectrum, Figure SI 12. There are two peaks, but the typical quadrupolar foot on the right-hand side has become a strong shoulder. The peak positions can be reproduced assuming δ_{iso} = 2.4 ppm, C_Q = 1.65 MHz, and $\eta \approx 0$. This is in agreement with the result reported by Pallister et al.[24]

The static ^{25}Mg spectrum of $MgCl_2$ is shown in Figure 4. The experimental spectrum cannot be simulated with the quadrupole parameters that follow from the MAS measurement. The resonance is significantly narrower, and the line shape differs as well. It is necessary to include a chemical shift anisotropy term (δ_{aniso}) of 8 ppm, see Figure 4. The other settings are η_{CSA} = 0.5 and $\alpha = \beta = \gamma = 0$. The simulation is very sensitive for δ_{aniso} and β but insensitive for the setting of η_{CSA}, α, and γ. The resulting simulation matches the peak positions and the general line shape very well. However, the intensity of the left peak in the simulation is higher than in the experimental spectrum.

DOI: 10.1021/acs.jpcc.5b12606
J. Phys. Chem. C 2016, 120, 6063−6074

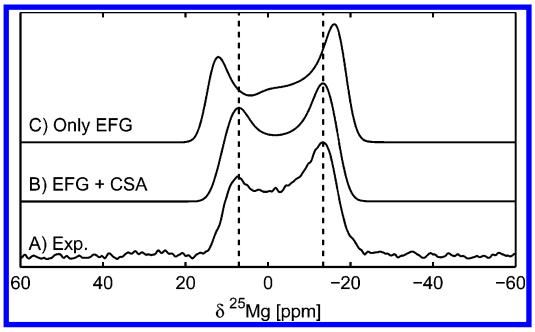

Figure 4. (A) Experimental 20 T static ^{25}Mg NMR spectra of $MgCl_2$. (B) Simulation including both EFG and CSA contribution. (C) Simulation including only EFG contribution as it follows from MAS experiment.

Ball Milling. In order to act as a support material in catalysis $MgCl_2$ is activated to get an enormous surface area. Reducing the particle size might have a significant influence on the structure and hence the NMR properties. Therefore, we studied ball-milled $MgCl_2$ as a first reference toward the support material in actual ZNCs.

The ^{35}Cl MAS NMR spectrum of $MgCl_2$ DM is shown in Figure 5. The well-defined quadrupolar features of $MgCl_2$ D are blurred. The peaks of $MgCl_2$ DM are considerably broader than those of $MgCl_2$ D, but the overall peak width has not increased. The static ^{35}Cl spectrum of $MgCl_2$ DM also shows a resonance that is broadened without losing the quadrupolar features completely, Figure 5. Again, the overall peak width has not increased. Noteworthy is the relatively steep discontinuity in the center of the spectrum. The ^{25}Mg NMR spectra of $MgCl_2$ DM show the same trend as the ^{35}Cl spectrum, see Figure SI 13 and 14.

DFT Calculations. To support the solid-state NMR findings, we performed DFT calculations of the ^{25}Mg and ^{35}Cl EFG tensor. Besides the bulk we also considered the most important surface sites. These are the basal (001) surface and the lateral (104) and (110) surfaces,[45−47] see Figure 6. The (001) surface exposes a plane of saturated Cl atoms and is therefore not considered relevant for catalysis. The (104) surface, exposing 5-coordinated Mg atoms, is more stable than the (110) surface, which exposes 4-coordinated Mg atoms. However, in the field of ZNC there is still a strong debate about which lateral facet coordinates the active titanium as the addition of organic adsorbates might change the picture.[48]

DFT calculations of the ^{35}Cl EFG are shown in Table 2 for the different functional and basis sets explored. Best results for the experimental bulk C_Q (4.6 MHz) are obtained with the

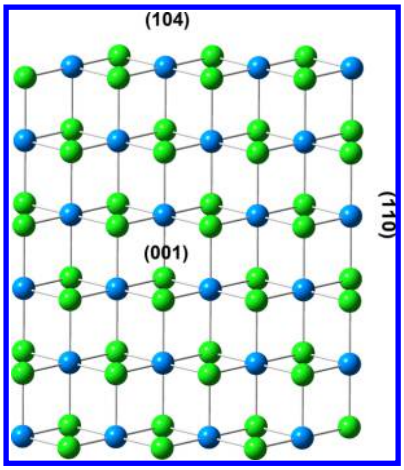

Figure 6. Fragment of a Cl−Mg−Cl layer showing the structure of the basal (001) and lateral (104) and (110) surfaces.

Table 2. DFT Calculations of the ^{35}Cl and ^{25}Mg Quadrupole Parameters for Different Species

		^{35}Cl		^{25}Mg	
level of theory	species	C_Q [MHz]	η	C_Q [MHz]	η
B3LYP-D2/TZVP	$MgCl_2$ bulk	6.3	0	1.97	0
	$MgCl_2$ (001)	5.6	0	1.93	0
	$MgCl_2$ (104)	−11.2	0.9	10.8	0.3
	$MgCl_2$ (110)	16.0	0.6	−15.6	0.3
PBE0-D2/TZVP	$MgCl_2$ bulk	5.6	0	1.83	0
	$MgCl_2$ (001)	5.0	0	1.84	0
	$MgCl_2$ (104)	10.5	1.0	11.1	0.3
	$MgCl_2$ (110)	15.7	0.6	−15.9	0.3
B3LYP-D2/pob-TZVP	$MgCl_2$ bulk	4.4	0	1.62	0
	$MgCl_2$ (001)	4.9	0	1.51	0
	$MgCl_2$ (104)	15.0	0.7	11.2	0.3
	$MgCl_2$ (110)	18.3	0.5	−16.6	0.4

B3LYP-D2/pob-TZVP level, but all functionals and basis sets show the same trend for the surface sites. They indicate large quadrupolar couplings for the (104) and (110) surface sites due to the lower symmetry of these surface sites, while the C_Q for the (001) site is comparable to the bulk. The coordination and symmetry of these surface atoms is quite similar to the bulk. While the B3LYP-D2/pob-TZVP level gives a slightly larger interaction strength, the other basis set (with both functionals) results in a slightly weaker quadrupole interaction compared to the bulk.

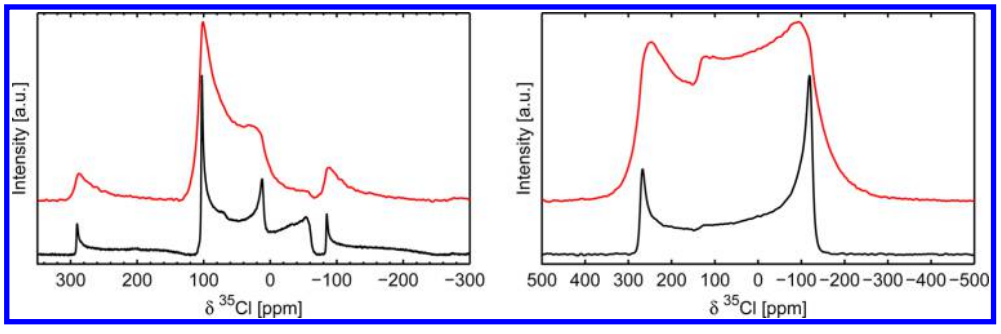

Figure 5. Static (right) and 15.625 kHz MAS (left) ^{35}Cl NMR spectra of $MgCl_2$ D (black) and $MgCl_2$ DM (red) obtained at 20 T at an RF field of 25 kHz using whole echo detection.

DOI: 10.1021/acs.jpcc.5b12606
J. Phys. Chem. C 2016, 120, 6063−6074

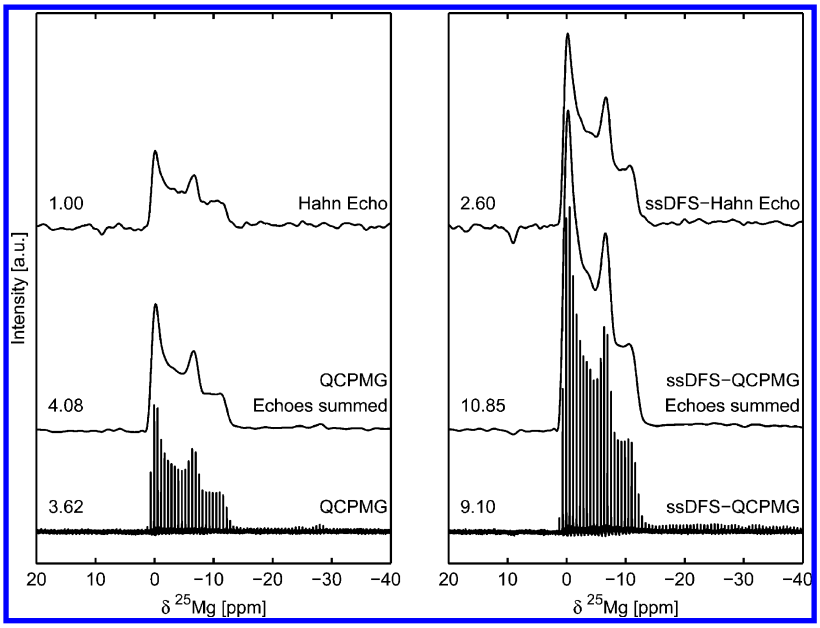

Figure 7. ^{25}Mg ssDFS-QCPMG NMR spectra of $MgCl_2$ at 15.625 kHz MAS at 20 T. Numbers on the right indicate the relative S/N ratios.

Table 2 also shows DFT calculations of the ^{25}Mg quadrupole parameters. The results show the same trend as for ^{35}Cl: the experimental bulk value is best reproduced at the B3LYP-D2/pob-TZVP level, (001) surface sites have quadrupolar parameters close to that of the bulk, and lateral surface sites have a distorted conformation leading to large C_Q.

Signal Enhancement. In order to increase the sensitivity of ^{25}Mg and ^{35}Cl, we worked on the implementation of signal enhancement schemes. Signal enhancement not only decreases experiment time but also can help in the observation of broad sites of low intensity, such as surface sites.

In particular, we combined the ssDFS[49] and QCPMG pulse sequences.[50−52] To optimize the ssDFS, we used tyrosine HCl as a reference sample for ^{35}Cl experiments. We reached a uniform enhancement of 1.90 (based on S/N). For $MgCl_2$ D, we obtained a lower enhancement of 1.6, probably due to the larger quadrupolar parameters. However, this still saves about a factor 2.5 in measurement time. Due to its higher spin quantum number, the enhancement for ^{25}Mg is theoretically larger. Indeed, we reached a uniform enhancement of 2.60 for the ^{25}Mg spectrum of $MgCl_2$ D, see Figure 7. The signal enhancement also works well for the ball-milled samples. For ^{25}Mg, a rather uniform enhancement of 2.47 was obtained. For ^{35}Cl, the enhancement was 1.53, Figure SI 15.

The crucial parameter for the enhancement is the offset of the ssDFS pulse, which determines the selection of the right pair of side bands. An optimization of this normally shows a modulation of the enhancement with a periodicity of the spinning speed. For tyrosine HCl we indeed observed this expected modulation. However, in the case of the ssDFS optimization for $MgCl_2$ (both ^{25}Mg and ^{35}Cl) we observed a periodic modulation not only of the intensity but also of the line shape. This effect was observed for the ball-milled samples as well.

The QCPMG enhancement depends on the spacing of the echoes as well as the T_2 of the sample, as this determines how many echoes can be acquired. $MgCl_2$ D proved to have a very long ^{25}Mg T_2 of 1.5 s, and hence, significant enhancements result from the QCPMG. An overall enhancement of more than 10 (based on S/N) is obtained when the ssDFS-QCPMG sequence is used, Figure 7. For ^{35}Cl we used some different QCPMG settings compared to ^{25}Mg, which enabled an enhancement of seven, see Figure SI 16. Together with ssDFS, again an overall enhancement of more than 10 is possible. QCPMG works also for static experiments, as shown in Figure SI 17 for $MgCl_2$ DCM. Again, an enhancement of about four is reached, which can be improved further by combining it with a regular DFS.

The experiment from Figure 7 used a total of 48 echoes with a 33 ms acquisition time each which were recorded in a total of 1.6 s acquisition time. The acquisition time of 33 ms makes sure that echoes are not truncated, and hence, an undistorted spectrum is obtained with an accurate description of the echo envelope due to the small spacing of the spikelets. It was acquired using 1024 scans with a recycle delay of 16 s, taking about 4.5 h of measurement time. Compared to the Hahn echo, the ssDFS-QCPMG showed an enhancement of about 10, making it possible to obtain meaningful spectra in a few minutes. By increasing the spikelet spacing, the enhancement can be pushed even further.

DISCUSSION

Proton Content. All $MgCl_2$ samples give a ^{1}H NMR signal; however, there are significant differences between the samples. While $MgCl_2$ DC and DCM show relatively narrow lines, $MgCl_2$ D and DM show a broad Pake doublet. The separation of the singularities of the Pake doublet corresponds to a proton−proton distance (r_{H-H}) of 1.65 Å. However, it can be seen that the Pake doublet is not symmetric, Figure 1. The right-hand foot is more pronounced than the left-hand foot. It was verified this was not caused by RF offset nor RF strength nor processing procedures. The asymmetry is caused by the contribution of a significant chemical shift anisotropy. The experimental spectrum can be simulated (see Figure 1E) when a CSA of around 20 ppm (6 kHz) is included, in agreement with typical values found in the literature for ice, gyspum, and silicates.[53−59] In the simulation, the PAS frames of both interaction tensors are aligned. It is also necessary to include 10

DOI: 10.1021/acs.jpcc.5b12606
J. Phys. Chem. C 2016, 120, 6063−6074

kHz of Gaussian line broadening to account for long-range dipolar couplings.

The r_{H-H} of 1.65 Å is longer than the distance found in the famous Pake doublet in gypsum[44] (r_{H-H} = 1.577 Å); however, other Pake doublets have been measured with shorter and longer distances.[57,60−62] The CSA indicates protons in an asymmetric environment. A distorted water conformation could account for the increased r_{H-H}. However, this is not in agreement with calculations. The adsorption of H_2O on $MgCl_2$ has been modeled,[43] and it did not show a distorted conformation. The r_{H-H} was calculated to be 1.551 Å for H_2O on (104) $MgCl_2$ and 1.573 Å for H_2O on (110) $MgCl_2$ (unpublished data from the study of Capone et al.[43]).

The narrower lines in the ^1H spectrum of the calcinated samples imply that the protons are either more mobile or more isolated compared to the protons in the chemically dried samples. This could, e.g., mean that the protons are no longer present as water but as surface hydroxyl groups. To ensure that the drying protocol did not alter the bulk structure, the samples were subjected to ^{25}Mg and ^{35}Cl NMR. The resulting spectra are comparable to the spectra obtained for $MgCl_2$ D and DM, indicating that the treatment left the bulk phase undisturbed. These samples were also investigated by XRD to test whether particles were annealed during heat treatment. Although a slight increase in particle size is observed, this does not seem to be an issue.

The ^1H MAS measurements unfortunately suffer from serious background and baseline problems due to the relatively low proton content of the samples. This makes these measurements nonquantitative, and therefore, we relied on static measurements performed in a home-built probe with no proton background for quantization. Also, the phasing and thus the chemical shift determination becomes more ambiguous. However, different samples in the MAS experiments can be directly compared to each other. From these measurements (see Figures 2 and SI 4) it is immediately clear that there is a big difference between the chemical nature of the residual protons in samples dried via the chemical protocol and the calcinated $MgCl_2$.

$MgCl_2$ D and DM show signals around 5 ppm, suggesting signal originating from H_2O. The resonances at 1.4 and 1.7 ppm in the MAS experiments of $MgCl_2$ DCM might very well correspond to Mg−OH groups.[59,63−65] Thus, both drying protocols result in samples that still give rise to a proton signal, however with a different chemical nature. XRD has shown the absence of hydrated phases; however, the quantification shows that there is the equivalent of a few percent (1−5%) H_2O per Mg atom. This suggests a full surface coverage of protonated groups (either Mg−H_2O or Mg−OH). When the $MgCl_2$ nanoparticles are prepared in the presence of organic donors, significantly smaller particles are obtained with much larger surface areas. However, here we do not observe large H_2O or OH signals, indicating that the binding of donors to the surface is stronger than that of protons, which is the subject of our current investigation.

Line Shape Analysis. The ^{25}Mg MAS and ^{35}Cl static experimental spectra of $MgCl_2$ have the same line shape as reported in the literature. However, our analysis of both the ^{25}Mg and the ^{35}Cl MAS and static line shapes point to an oversimplified interpretation in the literature. In both static spectra there is a difference in intensity for the left-hand side of the powder shape. In the case of MAS, the intensity difference concerns the whole resonance, with an emphasis on the right shoulder. An MQMAS experiment, field-dependent measurements, and ^{37}Cl measurements all prove that the line shape results from a single site and that the line shape is quadrupolar in nature. We conclude therefore that the spectrum must result from a nonideal powder.

Inspection of the $MgCl_2$ powder under a microscope revealed the presence of very small plate-shaped crystallites. Single-crystal XRD measurements showed that the crystallographic c axis is perpendicular to the plane of the platelets. This is in agreement with calculations by Busico et al.[46] and Credendino et al.,[47] who modeled the equilibrium crystallographic morphology of $MgCl_2$ particles. They showed flat particles, generally with a hexagonal shape, terminated by basal (001) planes. It can be envisioned that, under external force, some platelets stack on top of each other, giving a preferential alignment of the crystallites and hence a nonuniform powder pattern with nonrandom orientations.

We discovered that the preferred orientations we observe result from packing of the rotor. In order to get the maximal signal-to-noise ratio and stable spinning, a rotor should be filled tightly with a fine powder. A sample ("$MgCl_2$ D lp") was prepared by loosely filling the rotor, thus minimizing the chance of stacking of the platelets. As a result, the rotor contained almost 50% less sample, which reduces the signal-to-noise ratio. A preferred orientation is absent for this sample, however, as is proven by the regular quadrupolar powder pattern for the ^{35}Cl MAS NMR spectrum (Figure 9). Also, the ^{35}Cl static and ^{25}Mg MAS spectra show a regular quadrupolar pattern, while the ^{25}Mg static spectrum can be fitted by including both quadrupolar and chemical shift effects, see Figures SI 18−20. It can thus be concluded that the unusual line shape of $MgCl_2$ D is caused by a nonuniform powder distribution of the platelets.

To acquire more information about the distribution of orientations, we color coded the orientation of the z axis of the EFG tensor in relation to the resonance frequency obtained for that particular orientation in the spectrum (Figure 8). Note that

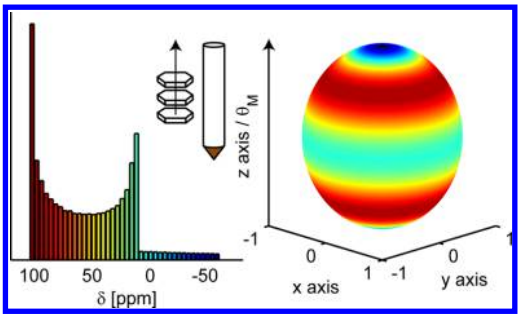

Figure 8. (Left) Orientation dependency of frequency intervals for a regular quadrupole powder pattern with η = 0 under fast magic angle spinning. (Right) Corresponding orientations of V_{ZZ} with respect to the MAS frame or rotor axis. Inset in the center schematically shows how platelets could stack in the rotor.

the representation of the sphere is valid in the MAS frame, meaning that the z axis aligns along the long axis of the rotor. Figure 8 shows that the low-intensity foot corresponds to the dark-blue orientations. These are crystallites for which the largest component of the quadrupolar tensor, V_{ZZ}, is oriented along the z axis of the MAS frame. These orientations are apparently preferred for $MgCl_2$ platelets, as the experimental intensity for these frequency domains is much higher than

DOI: 10.1021/acs.jpcc.5b12606
J. Phys. Chem. C 2016, 120, 6063−6074

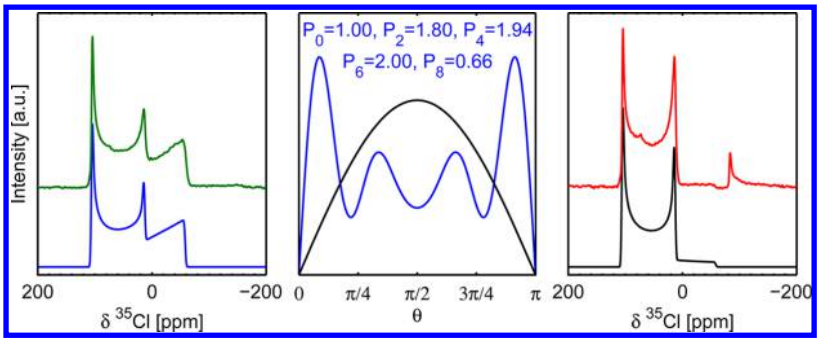

Figure 9. (Left) Experimental 20 T ^{35}Cl MAS spectrum of $MgCl_2$ D (green) and theoretical modeled spectrum (blue) using the ODF shown in the middel panel. (Middle) Normalized ODF's describing random orientation (black) and the specific orientation of $MgCl_2$ consisting of even term Legendre polynomials P_0–P_8 with the shown order parameters (blue). (Right) Experimental ^{35}Cl MAS spectrum of $MgCl_2$ D lp (red) and theoretical spectrum (black) corresponding to a random orientation. The feature around −85 ppm corresponds to a spinning side band.

would be expected. Crystallites for which V_{ZZ} is perpendicular to the z axis of the MAS frame (aquamarine-colored equator) occur less often, as can be seen from their lower intensity in the experimental spectrum.

To relate the quadrupole tensor to the molecular structure we have to look at the crystal structure of $MgCl_2$. α-$MgCl_2$ consists of Cl–Mg–Cl triple layers along the c axis. Each single layer has hexagonal symmetry in the ab plane. By definition, the c axis is perpendicular to this plane and is the unique axis. It can be inferred that V_{ZZ} is perpendicular to the ab plane as well and thus coincides with the c axis. The preferred orientations thus correspond to platelets stacked perpendicular to the rotor axis.

Above we described the preferred orientation in a qualitative way. By using order parameters we can describe the orientational preference in a more quantitative way, following the procedure by Van Gurp.[66] In general, an orientational distribution function (ODF) $f(\alpha, \beta, \gamma)$ expresses the possibility of finding an element with orientation (α, β, γ). Under the assumption of $\eta = 0$ we need to find a function that only depends on θ, where θ is defined as the angle between the z axis of the MAS frame and the z axis (V_{ZZ}) of the principal axis frame (PAS) of the quadrupolar interaction. For a random powder this function is $\sin(\theta)$. As shown by Van Gurp,[66] the distribution function can be described by a series expansion of spherical matrices. In the case of a uniaxial distribution, $\eta = 0$, the rotation matrices reduce to (even rank) Legendre polynomials.

The weighting factors of the individual Legendre polynomials ($\langle P_n \rangle$) are called order parameters. They control the ODF and hence ultimately describe the spectrum. For an isotropic distribution, all order parameters are zero with the exception of $\langle P_0 \rangle = 1$. Higher order terms must be included to account for the line shape of $MgCl_2$. We calculated subspectra for P_n and used singular value decomposition (SVD) to obtain the weighting factors. We included the (even) order parameters up to $\langle P_8 \rangle$. The corresponding distribution function that follows from this can be seen in Figure 9 along with a $\sin(\theta)$ function. It can be seen that orientations with a small angle θ occur more frequently. The difference between both functions gives the *preferred* orientation, see Figure SI 21.

Distribution of Quadrupole Interaction Parameters. The ^{35}Cl MAS NMR spectrum of $MgCl_2$ DM, Figure 5, is characteristic of a structure with a distribution in quadrupolar parameters. However, the distribution is relatively small, as the quadrupolar features can still be identified. A distribution of quadrupolar parameters fits in with the smaller particle size of $MgCl_2$ DM, with consequently more surface sites than $MgCl_2$ D. The peaks of $MgCl_2$ DM are considerably broader than those of $MgCl_2$ D, but the overall peak width has not increased. From the results in Figure 5 it seems that a preferred orientation is absent, but it cannot completely be ruled out. A control experiment in which $MgCl_2$ DM is loosely packed in a rotor shows that there actually still is a slight preferential orientation of V_{ZZ} parallel to the rotor axis for $MgCl_2$ DM when the rotor is tightly packed. It is far less pronounced than for $MgCl_2$ D, which can be expected given the much smaller particles.

Analysis of the static ^{35}Cl spectrum of $MgCl_2$ DM, Figure 5, corroborates the conclusions drawn from the MAS spectrum. The relatively steep step in the center of the spectrum clearly shows that a distribution in quadrupolar parameters is responsible for the spread out of the features instead of a dipolar (Gaussian) broadening. Also, a distribution in chemical shift parameters must be small. The ^{25}Mg NMR spectra of $MgCl_2$ DM corroborate the interpretation of the ^{35}Cl data.

Vittadello et al. described their ^{35}Cl spectrum of δ-$MgCl_2$ using a Lorentzian distribution for the quadrupolar coupling. This indeed gives an accurate description of the observed line shape; however, there is no physical background behind the model. The Czjzek model[67,68] is a physically sound model that can be used to describe a distribution in quadrupolar parameters for a disordered system. A so-called extended Czjzek model[69,70] has been introduced that models long-range disorder around a locally ordered site, e.g., it can describe the distribution of quadrupole parameters for a site that has an intrinsic quadrupole moment, which is the case for $MgCl_2$.

We fitted the distribution in the spectra of $MgCl_2$ DM to this extended Czjzek distribution using the EGdeconv program.[71] In this model $C_{Q,0}$ and η_0 are the quadrupolar parameters for the local order contribution. The distribution in quadrupolar parameters is described by the parameter σ, which corresponds to one-half the average quadrupolar product $\langle P_Q \rangle$ of the system. We obtained the following parameters: $C_{Q,0}$ = 4.34 MHz, $\eta_0 = 0$, and σ = 0.5 MHz (lower boundary for the fitting routine), see Figure SI 23. These results show how the average quadrupolar coupling parameter has decreased compared to the nonmilled sample. Vittadello et al.[42] also modeled their distributed site with a lower average quadrupolar coupling compared to α-$MgCl_2$. A lower average quadrupolar coupling can be explained by the contribution of (001) surface sites having slightly smaller quadrupolar coupling parameters than

DOI: 10.1021/acs.jpcc.5b12606
J. Phys. Chem. C 2016, 120, 6063–6074

the bulk. This is also indicated by our DFT calculations, Table 2.

Considering the size of the $MgCl_2$ nanoparticles (12−16 nm), we are most likely dealing with surface effects. It can be envisioned that sites in the vicinity of the surface feel a slightly different electric field gradient than the real bulk sites. Presumably there is a gradual transition in the quadrupole parameters going from the near-surface sites toward the "bulk". This would mean that the distribution is not completely random, and hence, the extended Czjzek distribution is not exactly designed for this system, which might give rise to some errors in the fitting.

As stated, $MgCl_2$ nanoparticles have relatively large surface areas. Terminations along the (001) direction expose saturated chlorides, and hence, these surfaces are not of interest for catalysis. The coordination is the same as in the bulk, and so we expect them to have similar quadrupole parameters as well as. This was indeed shown by our DFT calculations, Table 2. Terminations in the lateral dimension are perpendicular to the [104] and [110] directions and expose coordinatively unsaturated magnesium sites which are important for catalysis. The chlorine on these surfaces is no longer coordinated to three magnesium atoms but rather to two. Moreover, the magnesium atoms in question are also coordinatively unsaturated (pentacoordinated for (104), tetracoordinated for (110)). As a result, these surface sites deviate strongly from the bulk, which explains the large quadrupole couplings that we calculated for both magnesium and chlorine.

The quadrupole parameters calculated for the (104) and (110) surface sites correspond to static second-order line widths of the ^{35}Cl central transition of 300−600 and 600−850 kHz, respectively. Those are line widths which can no longer be averaged by MAS. Sites like these are also not readily observed in standard static experiments among others due to RF limitations. Moreover, since the surface sites represent only a fraction of the total spin pool, the spectrum will be dominated by the bulk and the broad lines are "lost" in the baseline. The corresponding line widths for the magnesium surface sites are 90−200 kHz. Compared to the <2 kHz line width of the bulk, these surface sites are also easily lost in regular ^{25}Mg experiments. An indirect method to infer the presence of surface sites for $MgCl_2$ nanoparticles is via the loss of bulk signal intensity.

Indeed, the intensity of the spectrum of $MgCl_2$ DM has decreased compared to $MgCl_2$ D. Both in the MAS and in the static spectrum, the relative intensity is 96% compared to $MgCl_2$ D. Assuming hexagonal particles with a size found from the XRD measurement (13 nm), the fraction of chlorine surface sites in $MgCl_2$ DM can be estimated. The fraction of unsaturated chlorine atoms on the lateral surfaces in $MgCl_2$ DM particles corresponds to 5%, which might suggest that we indeed lose these surface sites from the regular MAS and static spectra. The use of signal enhancement techniques might aid in the quest for the observation of broad sites with low intensity.

To this end, we report the static ^{25}Mg QCPMG spectrum of $MgCl_2$ DCM in Figure 10. This is acquired with an acquisition time per echo of 4 ms at an RF field strength of 20 kHz. The latter means that the central transition is not excited quantitatively anymore, which is also observed if Figure 10 is compared to Figure SI 16. However, a second component is visible in the spectrum between −350 and 200 ppm. This is the signal that probably points toward surface sites. However, the peak width of the static spectrum (±30 kHz) is much smaller

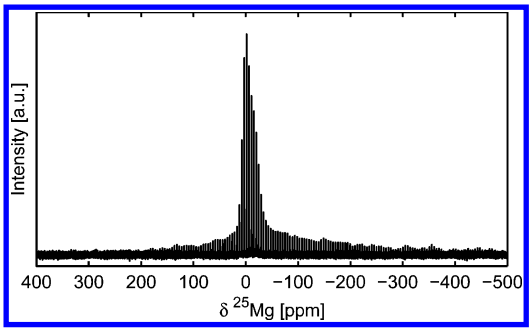

Figure 10. Static ^{25}Mg QCPMG spectrum of $MgCl_2$ DCM obtained at an RF field strength of 20 kHz.

than the corresponding line widths that follow from the calculations (90−200 kHz), Table 2. The applied RF field of is relatively low, restricting the excitation range of the QCPMG spectrum. The static QCPMG spectrum in Figure SI 16 is obtained with an RF field of 5 kHz, ensuring quantitative excitation of the central transition. Here the broad component spans only 20 kHz, indicating that indeed the available RF field strength is the limiting factor for detection of the broad component. Further investigations concentrating on static samples and broad-band excitation schemes are underway.

CONCLUSION

In this paper we reported on the study of $MgCl_2$ using ^{1}H, ^{25}Mg, and $^{35,37}Cl$ NMR. We prepared anhydrous $MgCl_2$ following a new protocol employing $SiCl_4$ or calcination. Hydrate phases were successfully removed, but the surfaces remained covered with protons. We showed how the morphology of $MgCl_2$ particles (plate-shaped crystallites) induces a preferred orientation when the sample is packed into the rotor, leading to a remarkable quadrupolar line shape. The orientation was quantified using order parameters. Having established the performance of enhancement schemes for ^{25}Mg and ^{35}Cl NMR and basis sets for DFT calculations, we plan to move forward to study more complex systems mimicking Ziegler−Natta catalysts.

Ball milling reduces the particle size, significantly leading to a distribution in quadrupole parameters for the bulk. In the nanoparticles surface sites represent a significant fraction of the total spin pool. The lateral surface sites are distorted, giving rise to large quadrupole parameters, which makes them invisible in regular static and MAS NMR spectra, which is observed as the decrease of overall signal intensity. This has important implications for catalyst particles as these have even larger surface areas. Further studies to characterize the broad surface sites are also needed, and they are the focus of our current investigations making use of $MgCl_2$ DM and binary adducts between $MgCl_2$ and organic electron donors.

EXPERIMENTAL SECTION

Sample Preparation. *$MgCl_2$ D.* We implemented a new protocol for the preparation of highly anhydrous $MgCl_2$ employing chemical drying with $SiCl_4$. Commercial "dry" $MgCl_2$ samples were suspended in heptane inside a Pyrex reactor with a sintered glass bottom filter, connected to a Schlenk line operating under flowing argon. A variable amount of $SiCl_4$ (0.3 to 3.3 M) was added, and the slurry was put under vigorous magnetic stirring at 55−65 °C. After a proper time (2−5 h), the liquid phase was siphoned out through the bottom

DOI: 10.1021/acs.jpcc.5b12606
J. Phys. Chem. C 2016, 120, 6063−6074

filter under vacuum. The solid was then washed with one or more aliquots of pentane at room temperature under vigorous stirring and finally dried under vacuum at 100 °C overnight.

$MgCl_2$ DC. Commercial dry $MgCl_2$ was calcinated by flowing it at 250 °C in a flow of dry N_2 for 6 h.

$MgCl_2$ DM and $MgCl_2$ DCM. After the above-described treatments, $MgCl_2$ D and $MgCl_2$ DC were physically activated by means of a Retsch PM-100 planetary ball mill equipped with an airtight chemically inert ceramic jar (Y-stabilized ZrO_2). The jar (internal volume of 50 mL) was loaded inside a glovebox along with 87 g of grinding balls (also made of ZrO_2, diameter 3 mm). The sealed jar was then transferred into the mill. The rotation speed was set to the 650 rpm (maximum value), and the rotation motion was inverted at 20 min intervals to prevent as far as possible encrustations on the inside walls of the jar. A milling time of 8 h turned out to be adequate to reach the minimum crystallite size (at longer times the primary particles start to coalesce).

Sample Characterization. Powder X-ray diffraction (XRD) was used to reveal the possible presence of crystalline $MgCl_2{\cdot}nH_2O$ phases in the dried samples. A Philips PW 1830 diffractometer, equipped with a custom-made airtight cell with PVC windows, able to maintain a static atmosphere with negligible O_2 and moisture contamination for at least 8 h has been used. The cell was loaded in a glovebox and transferred to the diffractometer, where the diffraction profile was collected using Ni-filtered Cu Kα radiation (20 mA, 40 kV) with a step scanning procedure (2θ range between 5° and 70°, 0.1° step, 20 s counting time per step). Powder XRD was also used to measure the average size of the primary particles for the ball-milled samples. No water reuptake was observed upon milling.

During the drying treatment, $SiCl_4$ will react with present H_2O to form SiO_2. This solid phase cannot be separated from the $MgCl_2$ phase. Using ICP-OES, the silicon content in the $MgCl_2$ DM sample was quantified as ∼5 wt %, corresponding to ∼10 wt % of SiO_2, assuming that all of the silicon is converted to silica. The quantification of the Mg content was in agreement with this number. EDS-TEM measurements were performed to investigate the distribution of silicon over the $SiCl_4$-dried $MgCl_2$. Unfortunately, it was not possible to avoid exposure to air during transfer of the sample into the JEOL 1010 TEM, with hydration and coagulation of particles as a result. Moreover, the copper grid used for analysis produced background signals in the Si EDS analysis. Nevertheless, the experiments do show that silicon is finely dispersed over the samples in small nanometer-sized spots. With the Si content not correlated to the Mg or Cl distribution, we concluded that silicon is not covering the surfaces of the $MgCl_2$ particles but form separate, probably SiO_2, particles of similar size as the $MgCl_2$ articles (see Figure SI 3).

Solid-State NMR Measurements. *Experimental Settings.* ^{25}Mg and ^{35,37}Cl spectra were recorded at room temperature on a Varian VNMRS 850 MHz spectrometer (20 T, 52.0 MHz for ^{25}Mg, 69.3 MHz for ^{37}Cl, 83.3 MHz for ^{35}Cl) using triple-resonance 4.0 mm and 1.6 mm Varian T3MAS probes at 15.625 or 31.250 kHz MAS. Typical RF fields were 25−30 kHz for ^{35}Cl and 5 kHz for ^{25}Mg to ensure quantitative excitation. Rotors were filled under inert nitrogen atmosphere inside a glovebox. Transfer time to the magnet was kept at the minimum, and during measurements the samples were constantly purged with a flow of dry nitrogen. Shifts were referenced to solid NaCl (δ_{iso} = −45.37 ppm with respect to infinitely dilute solution of NaCl(aq) (δ_{iso} = 0.0 ppm) or an aqueous MgCl solution (set to 0.0 ppm).

We used the side-band-selective double-frequency sweep (ssDFS) pulse scheme[49] to transfer population from the satellites into the central transition to increase the signal. A theoretical maximum enhancement of 2I can be obtained using ssDFS. For ^{25}Mg this implies an enhancement of 5, but it requires a single crystal. The enhancement for powder samples is lower and has been reported in the literature[49,72,73] between 2 and 3 for spin I = 5/2.

We also used the QCPMG detection scheme.[50−52] A series of echo pulses is applied with signal detection between the echoes. This leads to a so-called spikelet spectrum in which the regular Hahn-echo signal is split into a manifold of sharp lines (spikelets) which resemble the envelope of the echo spectrum. Since the intensity of the echo is distributed over a few spikelets, the signal-to-noise ratio increases significantly. As shown before,[27] we combined ssDFS and QCPMG to get maximum enhancement. For ^{35}Cl we used tyrosine HCl (C_Q = 2.23 MHz, η = 0.72, and δ_{iso} = 49.3 ppm[37]) to test the performance of the both sequences.

Proton measurements were performed on a 300 MHz spectrometer (7.04 T) using a home-built static probe without proton background. Either 4.0 mm rotors or glass tubes were used. Glass tubes were filled with $MgCl_2$ D and $MgCl_2$ DM in a glovebox and subsequently sealed in a flame to avoid contamination during measurements. The proton intensity was quantified against adamantane. Full T_2 decay curves have been obtained for each sample to account for T_2 relaxation effects. The T_2 curves have been fitted, and the pre-exponential factor has been taken as the quantitative intensity at τ = 0. MAS and fast MAS proton measurements were performed at 20 T (850 MHz) using 4.0 and 1.2 mm triple-resonance Varian T3MAS probes. To make sure that the proton signal and intensity are not misinterpreted, the rotor background was checked and/or the rotors were cleaned with ethanol.

Data Analysis. Nuclei with a spin larger than I = 1/2 possess an electric quadrupole moment (eQ). The interaction of the nuclear quadrupole moment (Q) with the electric field gradient (EFG) is described by the quadrupole coupling constant (C_Q) defined as $C_Q = e^2qQ/h$, in which $eq = V_{ZZ}$. The asymmetry of quadrupole tensor is defined as $\eta_Q = (V_{XX} - V_{YY})/V_{ZZ}$. Simulations of ideal quadrupolar line shapes are performed using SIMPSON.[74] This uses the Haeberlen convention for the chemical shift, in which the isotropic chemical shift is $\delta_{iso} = \frac{1}{3}(\delta_{xx} + \delta_{yy} + \delta_{zz})$. The chemical shift anisotropy and the asymmetry parameter are defined as $\delta_{aniso} = \delta_{zz} - \delta_{iso}$ and $\eta_{CSA} = (\delta_{yy} - \delta_{xx})/\delta_{aniso}$ with the principle values ordered according to $|\delta_{zz} - \delta_{iso}| \geq |\delta_{xx} - \delta_{iso}| \geq |\delta_{yy} - \delta_{iso}|$. The angles α, β, and γ give the relative orientation between the respective PAS frames of the chemical shift and the quadrupolar tensor.

Computational Details. All calculations were performed with the CRYSTAL09 package, a periodic ab initio program based on atom-centered (Gaussian) basis sets (LCAO approach).[75] The most stable α-form of $MgCl_2$ was considered. The surface of interest has been modeled using the slab approach as implemented in CRYSTAL code: slab models (2-D infinite systems) with translational symmetry in the *hkl* planes defining the surfaces are cut out of the previously optimized bulk structure.

All of the optimization and EFG calculations were carried out at the B3LYP[76] and PBE0[77] level, including Grimme's (D2)[78]

DOI: 10.1021/acs.jpcc.5b12606
J. Phys. Chem. C 2016, 120, 6063−6074

semiempirical correction for dispersion,[79] exploring two different triple-ζ valence plus polarization quality basis sets for the Cl atoms, namely, TZVP[80] and pob-TZVP,[81] whereas the TZVP basis set was always adopted for Mg atoms.

The positions of all atoms were always fully relaxed along with the cell parameters. With reference to the CRYSTAL09 user's manual,[75] in the evaluation of the Coulomb and Hartree−Fock exchange series, the five threshold parameters determining the level of accuracy were set at 7, 7, 7, 7, 14 values. The threshold on the SCF energy was set to 10^{-8} Ha. The reciprocal space was sampled according to a regular sublattice with a shrinking factor equal to 6.

■ ASSOCIATED CONTENT

Supporting Information

The Supporting Information is available free of charge on the ACS Publications website at DOI: 10.1021/acs.jpcc.5b12606.

XRD patterns before and after drying, and after ball milling, EDS-TEM images of $MgCl_2$ DM, additional ^{1}H, ^{25}Mg, and $^{35,37}Cl$ solid-state NMR spectra, analysis of the preferred orientation for static conditions and fit of the ^{35}Cl spectrum of $MgCl_2$ DM to the extended Czjzek model. (PDF)

■ AUTHOR INFORMATION

Corresponding Author

*E-mail: a.kentgens@nmr.ru.nl.

Notes

The authors declare no competing financial interest.

■ ACKNOWLEDGMENTS

This research forms part of the research programme of the Dutch Polymer Institute (DPI), project no. 793. The authors acknowledge T. van Kessel from the SABIC Research Center in Geleen, The Netherlands for the calcination of $MgCl_2$ and dr. P. Tinnemans from Radboud Univerisity for single-crystal XRD measurements. M.B. acknowledges the technical support with the SSNMR measurements provided by Gerrit Janssen, Hans Janssen, and Jan van Os. Support of the Dutch Organization for scientific research (NWO) for the "Solid state NMR facility for advanced materials science" in Nijmegen is gratefully acknowledged.

■ REFERENCES

(1) Kaminsky, W. *Polyolefins: 50 Years after Ziegler and Natta I Polyethylene and Polypropylene*, 1st ed.; Advances in Polymer Science; Springer-Verlag Berlin Heidelberg: Berlin, 2013; Vol. 257.

(2) Ziegler, K.; Holzkamp, E.; Breil, H.; Martin, H. The Mulheim Normal Pressure Polyethylene Process. *Angew. Chem.* **1955**, *67*, 541−547.

(3) Natta, G.; Pino, P.; Corradini, P.; Danusso, F.; Mantica, E.; Mazzanti, G.; Moraglio, G. Crystalline High Polymers of α-Olefins. *J. Am. Chem. Soc.* **1955**, *77*, 1708−1710.

(4) Kashiwa, N. The Discovery and Progress of $MgCl_2$-Supported $TiCl_4$ Catalysts. *J. Polym. Sci., Part A: Polym. Chem.* **2004**, *42*, 1−8.

(5) Partin, D.; O'Keeffe, M. The Structures and Crystal Chemistry of Magnesium Chloride and Cadmium Chloride. *J. Solid State Chem.* **1991**, *95*, 176−183.

(6) Galli, P.; Barbe, P.; Guidetti, G.; Zannetti, R.; Martorana, A.; Marigo, A.; Bergozza, M.; Fichera, A. The Activation of $MgCl_2$-Supported Ziegler-Natta Catalysts - A Structural Investigation. *Eur. Polym. J.* **1983**, *19*, 19−24.

(7) Gerbasi, R.; Marigo, A.; Martorana, A.; Zannetti, R.; Guidetti, G. P.; Baruzzi, G. The Activation of $MgCl_2$-Supported Ziegler-Natta Catalysts. 2. Correlation between Activity and Structural Disorder. *Eur. Polym. J.* **1984**, *20*, 967−970.

(8) Giunchi, G.; Allegra, G. Structural Disorder in Microcrystalline $MgCl_2$. *J. Appl. Crystallogr.* **1984**, *17*, 172−178.

(9) Di Noto, V.; Pavanello, L.; Viviani, M.; Storti, G.; Bresadola, S. A Kinetic Investigation of Ethyl Formate Elimination from the $[MgCl_2(HCOOC_2H_5)_2]_n$ Adduct using Thermoanalytical Data. *Thermochim. Acta* **1991**, *189*, 223−233.

(10) Di Noto, V.; Marigo, A.; Viviani, M.; Marega, C.; Bresadola, S.; Zannetti, R. $MgCl_2$-Supported Ziegler-Natta Catalysts - Synthesis and X-Ray-Diffraction Characterization of Some $MgCl_2$-Lewis Base Adducts. *Makromol. Chem.* **1992**, *193*, 123−131.

(11) Di Noto, V.; Zannetti, R.; Vivani, M.; Marega, C.; Marigo, A.; Bresadola, S. $MgCl_2$-Supported Ziegler-Natta Catalysts - A Structural Investigation by X-Ray Diffraction and Fourier-Transform IR Spectroscopy on the Chemical Activation Process through $MgCl_2$-Ethanol Adducts. *Makromol. Chem.* **1992**, *193*, 1653−1663.

(12) Di Noto, V.; Bresadola, S. New Synthesis of a Highly Active δ-$MgCl_2$ for $MgCl_2/TiCl_4/AlEt_3$ Catalytic Systems. *Macromol. Chem. Phys.* **1996**, *197*, 3827−3835.

(13) Dupree, R.; Smith, M. E. Solid-State Magnesium-25 NMR Spectroscopy. *J. Chem. Soc., Chem. Commun.* **1988**, 1483−1485.

(14) MacKenzie, K. J. D.; Meinhold, R. H.; Sherriff, B. L.; Xu, Z. ^{27}Al and ^{25}Mg Solid-State Magic-Angle Spinning Nuclear Magnetic Resonance Study of Hydrotalcite and Its Thermal Decomposition Sequence. *J. Mater. Chem.* **1993**, *3*, 1263−1269.

(15) MacKenzie, K.; Meinhold, H. ^{25}Mg Nuclear Magnetic Resonance Spectroscopy of Minerals and Related Inorganics: A Survey Study. *Am. Mineral.* **1994**, *79*, 250−260.

(16) MacKenzie, K.; Meinhold, H. MAS NMR Study of Pentacoordinated Magnesium in Grandidierite. *Am. Mineral.* **1997**, *82*, 479−482.

(17) Kroeker, S.; Stebbins, J. F. Magnesium Coordination Environments in Glasses and Minerals: New Insight from High-Field ^{25}Mg MAS NMR. *Am. Mineral.* **2000**, *85*, 1459−1464.

(18) Kroeker, S.; Neuhoff, P. S.; Stebbins, J. F. Enhanced Resolution and Quantitation from 'Ultrahigh' Field NMR Spectroscopy of Glasses. *J. Non-Cryst. Solids* **2001**, *293*−*295*, 440−445.

(19) Shimoda, K.; Nemoto, T.; Saito, K. Local Structure of Magnesium in Silicate Glasses: A ^{25}Mg 3QMAS NMR Study. *J. Phys. Chem. B* **2008**, *112*, 6747−6752.

(20) Sen, S.; Maekawa, H.; Papatheodorou, G. N. Short-Range Structure of Invert Glasses along the Pseudo-Binary Join $MgSiO_3$-Mg_2SiO_4: Results from ^{29}Si and ^{25}Mg MAS NMR Spectroscopy. *J. Phys. Chem. B* **2009**, *113*, 15243−15248.

(21) Bastow, T.; Celotto, S. ^{25}Mg NMR Site Analysis in Metals and Intermetallics. *Solid State Nucl. Magn. Reson.* **2009**, *35*, 217−222.

(22) Wu, G.; Wong, A.; Wang, S. Solid-state ^{25}Mg NMR, X-Ray Crystallographic, and Quantum Mechanical Study of Bis(pyridine)-(5,10,15,20-tetraphenylporphyrinato)magnesium(II). *Can. J. Chem.* **2003**, *81*, 275−283.

(23) Cahill, L. S.; Hanna, J. V.; Wong, A.; Freitas, J. C. C.; Yates, J. R.; Harris, R. K.; Smith, M. E. Natural Abundance ^{25}Mg Solid-State NMR of Mg Oxyanion Systems: A Combined Experimental and Computational Study. *Chem. - Eur. J.* **2009**, *15*, 9785−9798.

(24) Pallister, P. J.; Moudrakovski, I. L.; Ripmeester, J. A. Mg-25 Ultra-High Field Solid State NMR Spectroscopy and First Principles Calculations of Magnesium Compounds. *Phys. Chem. Chem. Phys.* **2009**, *11*, 11487−11500.

(25) Burgess, K. M. N.; Xu, Y.; Leclerc, M. C.; Bryce, D. L. Insight into Magnesium Coordination Environments in Benzoate and Salicylate Complexes through ^{25}Mg Solid-State NMR Spectroscopy. *J. Phys. Chem. A* **2013**, *117*, 6561−6570.

(26) Xu, J.; Terskikh, V. V.; Huang, Y. Resolving Multiple Non-Equivalent Metal Sites in Magnesium-Containing Metal-Organic Frameworks by Natural Abundance ^{25}Mg Solid-State NMR Spectroscopy. *Chem. - Eur. J.* **2013**, *19*, 4432−4436.

DOI: 10.1021/acs.jpcc.5b12606
J. Phys. Chem. C 2016, 120, 6063−6074

(27) Blaakmeer, E. S.; Rosciano, F.; van Eck, E. R. H. Lithium Doping of $MgAl_2O_4$ and $ZnAl_2O_4$ Investigated by High-Resolution Solid State NMR. *J. Phys. Chem. C* **2015**, *119*, 7565−7577.
(28) O'Keefe, C. A.; Johnston, K. E.; Sutter, K.; Autschbach, J.; Gauvin, R.; Trébosc, J.; Delevoye, L.; Popoff, N.; Taoufik, M.; Oudatchin, K.; et al. An Investigation of Chlorine Ligands in Transition-Metal Complexes via ^{35}Cl Solid-State NMR and Density Functional Theory Calculations. *Inorg. Chem.* **2014**, *53*, 9581−9597.
(29) Johnston, K. E.; O'Keefe, C. A.; Gauvin, R. M.; Trébosc, J.; Delevoye, L.; Amoureux, J.-P.; Popoff, N.; Taoufik, M.; Oudatchin, K.; Schurko, R. W. A Study of Transition-Metal Organometallic Complexes Combining ^{35}Cl Solid-State NMR Spectroscopy and ^{35}Cl NQR Spectroscopy and First-Principles DFT Calculations. *Chem. - Eur. J.* **2013**, *19*, 12396−12414.
(30) Perić, B.; Gautier, R.; Pickard, C. J.; Bosiočić, M.; Grbić, M. S.; Požek, M. Solid-State NMR/NQR and First-Principles Study of Two Niobium Halide Cluster Compounds. *Solid State Nucl. Magn. Reson.* **2014**, *59*−*60*, 20−30.
(31) Hanson, M. A.; Terskikh, V. V.; Baines, K. M.; Huang, Y. Chlorine-35 Solid-State NMR Spectroscopy as an Indirect Probe of Germanium Oxidation State and Coordination Environment in Germanium Chlorides. *Inorg. Chem.* **2014**, *53*, 7377−7388.
(32) Perras, F. A.; Bryce, D. L. Direct Investigation of Covalently Bound Chlorine in Organic Compounds by Solid-State ^{35}Cl NMR Spectroscopy and Exact Spectral Line-Shape Simulations. *Angew. Chem., Int. Ed.* **2012**, *51*, 4227−4230.
(33) Chapman, R. P.; Widdifield, C. M.; Bryce, D. L. Solid-State NMR of Quadrupolar Halogen Nuclei. *Prog. Nucl. Magn. Reson. Spectrosc.* **2009**, *55*, 215−237.
(34) Weeding, T. L.; Veeman, W. S. Characterization of the Structure of Inorganic Chloride Salts with Chlorine Solid-State NMR. *J. Chem. Soc., Chem. Commun.* **1989**, 946−948.
(35) Bryce, D. L.; Bultz, E. B. Alkaline Earth Chloride Hydrates: Chlorine Quadrupolar and Chemical Shift Tensors by Solid-State NMR Spectroscopy and Plane Wave Pseudopotential Calculations. *Chem. - Eur. J.* **2007**, *13*, 4786−4796.
(36) Skibsted, J.; Jakobsen, H. J. ^{35}Cl and ^{37}Cl Magic-Angle Spinning NMR Spectroscopy in the Characterization of Inorganic Perchlorates. *Inorg. Chem.* **1999**, *38*, 1806−1813.
(37) Bryce, D. L.; Gee, M.; Wasylishen, R. E. High-Field Chlorine NMR Spectroscopy of Solid Organic Hydrochloride Salts: A Sensitive Probe of Hydrogen Bonding Environment. *J. Phys. Chem. A* **2001**, *105*, 10413−10421.
(38) Honda, H. Even-Odd Effect of ^{35}Cl Quadrupole Coupling Constants in Solid n-Alkylammonium Chlorides (C_5-C_{10}). *Z. Naturforsch., A: Phys. Sci.* **2003**, *58*, 623−630.
(39) Gervais, C.; Dupree, R.; Pike, K. J.; Bonhomme, C.; Profeta, M.; Pickard, C. J.; Mauri, F. Combined First-Principles Computational and Experimental Multinuclear Solid-State NMR Investigation of Amino Acids. *J. Phys. Chem. A* **2005**, *109*, 6960−6969.
(40) Bryce, D. L.; Sward, G. D. Chlorine-35/37 NMR Spectroscopy of Solid Amino Acid Hydrochlorides: Refinement of Hydrogen-Bonded Proton Positions using Experiment and Theory. *J. Phys. Chem. B* **2006**, *110*, 26461−26470.
(41) Bryce, D. L.; Sward, G. D.; Adiga, S. Solid-State $^{35/37}$Cl NMR Spectroscopy of Hydrochloride Salts of Amino Acids Implicated in Chloride Ion Transport Channel Selectivity: Opportunities at 900 MHz. *J. Am. Chem. Soc.* **2006**, *128*, 2121−2134.
(42) Vittadello, M.; Stallworth, P. E.; Alamgir, F. M.; Suarez, S.; Abbrent, S.; Drain, C. M.; Di Noto, V.; Greenbaum, S. G. Polymeric δ-$MgCl_2$ Nanoribbons. *Inorg. Chim. Acta* **2006**, *359*, 2513−2518.
(43) Capone, F.; Rongo, L.; D'Amore, M.; Budzelaar, P. H. M.; Busico, V. Periodic Hybrid DFT Approach (Including Dispersion) to $MgCl_2$-Supported Ziegler-Natta Catalysts. 2. Model Electron Donor Adsorption on $MgCl_2$ Crystal Surfaces. *J. Phys. Chem. C* **2013**, *117*, 24345−24353.
(44) Pake, G. E. Nuclear Resonance Absorption in Hydrated Crystals: Fine Structure of the Proton Line. *J. Chem. Phys.* **1948**, *16*, 327−336.
(45) Corradini, P.; Barone, V.; Fusco, R.; Guerra, G. A Possible Model of Catalytic Sites for the Stereospecific Polymerization of α-Olefins on 1st Generation and Supported Ziegler-Natta Catalysts. *Gazz. Chim. Ital* **1983**, *113*, 601−607.
(46) Busico, V.; Causa, M.; Cipullo, R.; Credendino, R.; Cutillo, F.; Friederichs, N.; Lamanna, R.; Segre, A.; Van Axel Castelli, V. Periodic DFT and High-Resolution Magic-Angle-Spinning (HR-MAS) ^{1}H NMR Investigation of the Active Surfaces of $MgCl_2$-Supported Ziegler-Natta Catalysts. The $MgCl_2$ Matrix. *J. Phys. Chem. C* **2008**, *112*, 1081−1089.
(47) Credendino, R.; Busico, V.; Causá, M.; Barone, V.; Budzelaar, P. H. M.; Zicovich-Wilson, C. Periodic DFT Modeling of Bulk and Surface Properties of $MgCl_2$. *Phys. Chem. Chem. Phys.* **2009**, *11*, 6525−6532.
(48) Credendino, R.; Liguori, D.; Fan, Z.; Morini, G.; Cavallo, L. Toward a Unified Model Explaining Heterogeneous Ziegler-Natta Catalysis. *ACS Catal.* **2015**, *5*, 5431−5435.
(49) Goswami, M.; van Bentum, P.; Kentgens, A. Sensitivity Enhancement in MAS NMR of Half-Integer Quadrupolar Nuclei using Sideband Selective Double-Frequency Sweeps. *Can. J. Chem.* **2011**, *89*, 1130−1137.
(50) Larsen, F. H.; Jakobsen, H. J.; Ellis, P. D.; Nielsen, N. C. Sensitivity-Enhanced Quadrupolar-Echo NMR of Half-Integer Quadrupolar Nuclei. Magnitudes and Relative Orientation of Chemical Shielding and Quadrupolar Coupling Tensors. *J. Phys. Chem. A* **1997**, *101*, 8597−8606.
(51) Larsen, F. H.; Jakobsen, H. J.; Ellis, P. D.; Nielsen, N. C. QCPMG-MAS NMR of Half-Integer Quadrupolar Nuclei. *J. Magn. Reson.* **1998**, *131*, 144−147.
(52) Larsen, F. H.; Skibsted, J.; Jakobsen, H. J.; Nielsen, N. C. Solid-State QCPMG NMR of Low-γ Quadrupolar Metal Nuclei in Natural Abundance. *J. Am. Chem. Soc.* **2000**, *122*, 7080−7086.
(53) Pfrommer, B. G.; Mauri, F.; Louie, S. G. NMR Chemical Shifts of Ice and Liquid Water: The Effects of Condensation. *J. Am. Chem. Soc.* **2000**, *122*, 123−129.
(54) Hinton, J.; Guthrie, P.; Pulay, P.; Wolinski, K. Ab Initio Quantum-Mechanical Chemical-Shift Calculations for the ^{29}Si Nucleus in a Variety of Compounds. *J. Magn. Reson., Ser. A* **1993**, *103*, 188−190.
(55) Pines, A.; Ruben, D. J.; Vega, S.; Mehring, M. New Approach to High-Resolution Proton NMR in Solids: Deuterium Spin Decoupling by Multiple-Quantum Transitions. *Phys. Rev. Lett.* **1976**, *36*, 110−113.
(56) Burum, D.; Rhim, W. Proton NMR Study of Gypsum, $CaSO_4 \cdot 2H_2O$, Using an Improved Technique for Homonuclear Dipolar Decoupling in Solids. *J. Magn. Reson.* **1979**, *34*, 241−246.
(57) Riemer, T.; Schmidt, B.; Behrens, H.; Dupree, R. H_2O/OH Ratio Determination in Hydrous Aluminosilicate Glasses by Static Proton NMR and the Effect of Chemical Shift Anisotropy. *Solid State Nucl. Magn. Reson.* **2000**, *15*, 201−207.
(58) Schmidt, B.; Behrens, H.; Riemer, T.; Kappes, R.; Dupree, R. Quantitative Determination of Water Speciation in Aluminosilicate and Glasses: A Comparative NMR and IR Spectroscopic Study. *Chem. Geol.* **2001**, *174*, 195−208.
(59) Phillips, B. L.; Burnley, P. C.; Worminghaus, K.; Navrotsky, A. Si-29 and H-1 NMR Spectroscopy of High-Pressure Hydrous Magnesium Silicates. *Phys. Chem. Miner.* **1997**, *24*, 179−190.
(60) Kuhns, P. L.; Richter, L. J.; Conradi, M. S. Proton NMR-Study of the Orientation and Motion of H_2O in Na β" Alumina. *J. Chem. Phys.* **1982**, *76*, 6−9.
(61) Simakin, A. G.; Salova, T. P.; Zavelsky, V. O. Mechanism of Water Dissolution in Sodium-Silicate Melts and Glasses: Structural Interpretation of Spectroscopic Data. *Geochem. Int.* **2008**, *46*, 107−115.
(62) Totland, C.; Steinkopf, S.; Blokhus, A. M.; Nerdal, W. Water Structure and Dynamics at a Silica Surface: Pake Doublets in H-1 NMR Spectra. *Langmuir* **2011**, *27*, 4690−4699.
(63) Xue, X.; Kanzaki, M. High-Pressure δ-$Al(OH)_3$ and δ-AlOOH Phases and Isostructural Hydroxides/Oxyhydroxides: New Structural

DOI: 10.1021/acs.jpcc.5b12606
J. Phys. Chem. C 2016, 120, 6063−6074

Insights from High-Resolution H-1 and Al-27 NMR. *J. Phys. Chem. B* **2007**, *111*, 13156−13166.
(64) Xue, X.; Kanzaki, M.; Shatskiy, A. Dense Hydrous Magnesium Silicates, Phase D, and Superhydrous B: New Structural Constraints from One- and Two-Dimensional ^{29}Si and ^{1}H NMR. *Am. Mineral.* **2008**, *93*, 1099−1111.
(65) Xue, X.; Kanzaki, M. Proton Distributions and Hydrogen Bonding in Crystalline and Glassy Hydrous Silicates and Related Inorganic Materials: Insights from High-Resolution Solid-State Nuclear Magnetic Resonance Spectroscopy. *J. Am. Ceram. Soc.* **2009**, *92*, 2803−2830.
(66) van Gurp, M. The Use of Rotation Matrices in the Mathematical Description of Molecular Orientations in Polymers. *Colloid Polym. Sci.* **1995**, *273*, 607−625.
(67) Czjzek, G.; Fink, J.; Götz, F.; Schmidt, H.; Coey, J. M. D.; Rebouillat, J.-P.; Liénard, A. Atomic Coordination and the Distribution of Electric Field Gradients in Amorphous Solids. *Phys. Rev. B: Condens. Matter Mater. Phys.* **1981**, *23*, 2513−2530.
(68) d'Espinose de Lacaillerie, J.-B.; Fretigny, C.; Massiot, D. MAS NMR Spectra of Quadrupolar Nuclei in Disordered Solids: The Czjzek Model. *J. Magn. Reson.* **2008**, *192*, 244−51.
(69) Le Caër, G.; Bureau, B.; Massiot, D. An Extension of the Czjzek Model for the Distributions of Electric Field Gradients in Disordered Solids and an Application to NMR Spectra of ^{71}Ga in Chalcogenide Glasses. *J. Phys.: Condens. Matter* **2010**, *22*, 065402.
(70) Knijn, P. J.; van Bentum, P. J. M.; van Eck, E. R. H.; Fang, C.; Grimminck, D. L. A. G.; de Groot, R. A.; Havenith, R. W. A.; Marsman, M.; Meerts, W. L.; de Wijs, G. A.; et al. A Solid-State NMR and DFT Study of Compositional Modulations in $Al_xGa_{1-x}As$. *Phys. Chem. Chem. Phys.* **2010**, *12*, 11517−11535.
(71) Grimminck, D. L.; Polman, B. J.; Kentgens, A. P.; Leo Meerts, W. EASY-GOING Deconvolution: Combining Accurate Simulation and Evolutionary Algorithms for Fast Deconvolution of Solid-State Quadrupolar NMR Spectra. *J. Magn. Reson.* **2011**, *211*, 114−120.
(72) Goswami, M.; van Bentum, P. J. M.; Kentgens, A. P. M. Repetitive Sideband-Selective Double Frequency Sweeps for Sensitivity Enhancement of MAS NMR of Half-Integer Quadrupolar Nuclei. *J. Magn. Reson.* **2012**, *219*, 25−32.
(73) Perras, F. A.; Viger-Gravel, J.; Burgess, K. M. N.; Bryce, D. L. Signal Enhancement in Solid-State NMR of Quadrupolar Nuclei. *Solid State Nucl. Magn. Reson.* **2013**, *51*−*52*, 1−15.
(74) Bak, M.; Rasmussen, J. T.; Nielsen, N. C. SIMPSON: A General Simulation Program for Solid-State NMR Spectroscopy. *J. Magn. Reson.* **2000**, *147*, 296−330.
(75) Dovesi, R.; Saunders, V. R.; Orlando, R.; Zicovich-Wilson, C. M.; Pascale, F.; Civalleri, B.; Doll, K.; Bush, I. J.; D'Arco, P.; Lunell, M. *Crystal 2009 User Manual*; Turin University, Turin, 2009.
(76) Becke, A. D. Density-Functional Thermochemistry. III. The Role of Exact Exchange. *J. Chem. Phys.* **1993**, *98*, 5648−5652.
(77) Adamo, C.; Barone, V. Toward Reliable Density Functional Methods without Adjustable Parameters: The PBE0Model. *J. Chem. Phys.* **1999**, *110*, 6158−6170.
(78) Grimme, S. Semiempirical GGA-Type Density Functional Constructed with a Long-Range Dispersion Correction. *J. Comput. Chem.* **2006**, *27*, 1787−1799.
(79) Civalleri, B.; Zicovich-Wilson, C. M.; Valenzano, L.; Ugliengo, P. B3LYP Augmented with an Empirical Dispersion Term (B3LYP-D*) as Applied to Molecular Crystals. *CrystEngComm* **2008**, *10*, 405−410.
(80) D'Amore, M.; Credendino, R.; Budzelaar, P. H.; Causá, M.; Busico, V. A Periodic Hybrid DFT Approach (Including Dispersion) to $MgCl_2$-Supported Ziegler-Natta catalysts - 1: $TiCl_4$ Adsorption on $MgCl_2$ Crystal Surfaces. *J. Catal.* **2012**, *286*, 103−110.
(81) Peintinger, M. F.; Oliveira, D. V.; Bredow, T. Consistent Gaussian Basis Sets of Triple-Zeta Valence with Polarization Quality for Solid-State Calculations. *J. Comput. Chem.* **2013**, *34*, 451−459.

DOI: 10.1021/acs.jpcc.5b12606
J. Phys. Chem. C 2016, 120, 6063−6074